Mehdi Dali
Jamel Belhadj
Xavier Roboam

Regular paper

Design of a stand-alone hybrid Photovoltaic-Wind generating system with battery storage

- ***Energy based modeling with losses integration***
- ***Energy management control strategy***

In this paper the authors have developed an isolated network for very low voltage (VLV) decentralized energy production and storage based on renewable energy (hybrid system: photovoltaic and wind). An energy based model of stand-alone hybrid photovoltaic-wind generating system is presented, using bond graph approach. An equivalent average modeling of a hybrid photovoltaic-wind generating system is used. The modeling of the components of the global system is developed with the integration of converters losses involved in the solar and wind generating subsystems. It is shown that this model is interesting for analyzing the dynamic behavior of the system and for designing the control strategy. The energy management and control of the photovoltaic and wind subsystems are based on voltage and current control with Maximum Power Point Tracking (MPPT) allowing the optimal transfer of power to DC load.

Keywords: Hybrid system; photovoltaic energy; wind energy; battery storage; system modeling; converter losses; Bond graph; Control strategies.

1. INTRODUCTION

The rising rate of consumption and the price of fossil fuels and the environmental problems caused by the conventional power generation draw worldwide attention to renewable energy technologies. In fact, renewable energy systems are pollution free, takes low cost and less gestation period, user and social friendly. However, renewable power unit based on single source (wind or solar source) may not be effective in terms of cost, efficiency and reliability. A viable alternative solution is by combining these different renewable energy sources to form a hybrid energy system [1, 2]. Hybrid energy system is an excellent solution for electrification of remote rural areas where the grid extension is difficult and not economical. Such system incorporates a combination of several renewable energy sources such as solar photovoltaic, wind energy and may be conventional generators for backup. A system using a combination of these different sources has the advantage of balance and stability that offers the strengths of each type of sources that complement one another. The main objective is to provide 24 hours demand quality power in remote communities. Hybrid systems can provide electricity at a comparatively economic price in many remote areas. In order to obtain electricity from a hybrid system reliably and at an economical price, its design must be optimal in terms of operation, control and component selection. Many topologies are available for hybrid systems, depending on interface converters between the sources and the interconnection DC bus (Low DC voltage "LV", Very Low DC voltage "VLV" loads). We have investigated to design an optimum architecture of hybrid system with Very Low Voltage (VLV) DC (48V). With this DC bus, this stand-alone hybrid system can be implemented into rural or urban areas [3], [4]. Such systems are used today in many applications as battery charging, water pumping and desalination [5-7].

This paper aims at the averaged modeling and energy flow analysis of a stand-alone hybrid generating system comprising of wind and photovoltaic subsystems. The average model is used because it's adequate for long time dynamic simulations. Both, photovoltaic

and wind conversion subsystems are modeled and simulated integrating chopper losses. A mathematical modeling and analysis of energy losses involved with power conditioners converters is particularly developed. As well, the design and the dimensioning of Buck power components (inductor, capacitor) are presented for each subsystem.

Hybrid system is clearly a multidisciplinary system. In order to model such a system, the authors have chosen an energy based approach. This approach consists in defining and modeling the energy couplings and the energy exchanges within the system. We have applied it via the Bond Graph formalism which is an explicit graphical tool for describing energy exchanges within a system [8]. Allowing a unified representation of the laws of the various fields of physics, Bond Graph can moreover facilitate multidisciplinary exchanges.

Maximum power point tracking (MPPT) controllers are used in photovoltaic (PV) and wind subsystems to maximize respectively the photovoltaic array and the wind generator output powers, irrespective of the climatic conditions (temperature, irradiation and the wind velocity) and of the load electrical characteristics.

The individual systems are simulated for varying wind velocities and solar intensities respectively and the results are used to identify the performances of hybrid system.

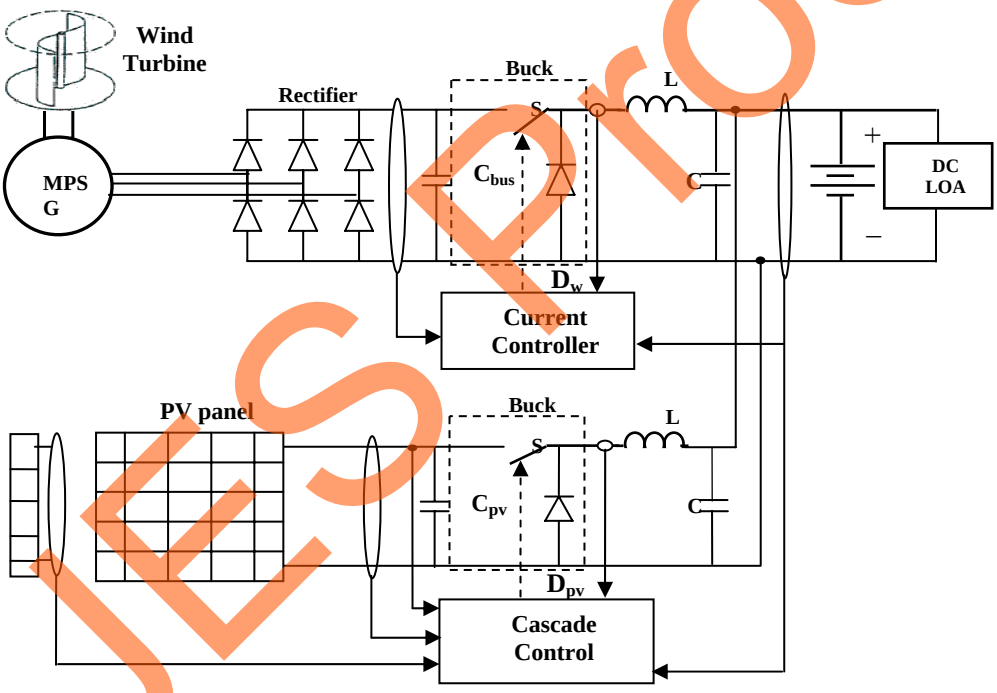

Fig. 1 : Hybrid photovoltaic - wind generating system with VLV DC bus.

2. HYBRID WIND-PHOTOVOLTAIC GENERATING SYSTEM

Fig. 1 shows the scheme of the hybrid wind-photovoltaic generating system with very low voltage (VLV) DC bus (48V) considered in this paper [3, 4].The variable output voltage of the photovoltaic generator is also controlled by a DC/DC buck converter. The variable voltage and frequency of the wind driven permanent magnet synchronous generator (PMSG) is first rectified and controlled by a DC/DC buck converter. The DC bus collects the total power from the wind and photovoltaic systems and uses it partly to

supply the required load demand and partly to charge the battery bank. The photovoltaic and wind subsystems modeling are described as follows.

3. PHOTOVOLTAIC GENERATING SUBSYSTEM

Fig. 2 shows the block diagram of the PV subsystem proposed in this paper. The PV array used deliver 400 W peak power (V_p=75.5 V and I_p=5.5 A at 1 kW/m² and 25°C). To satisfy the required DC load and the 48V battery voltage level, buck DC/DC chopper must be controlled to extract the maximum power from the photovoltaic generator.

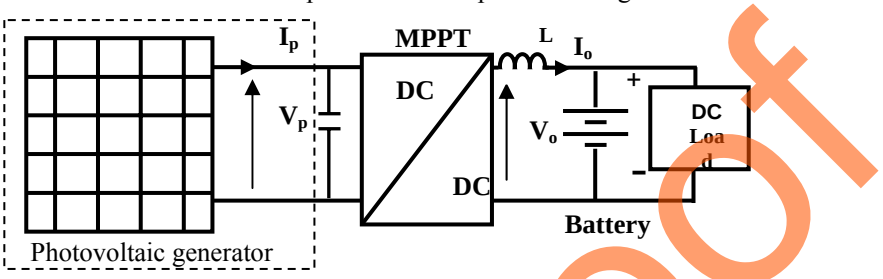

Fig. 2 : Photovoltaic generating subsystem.

This is obtained with a Maximum Power Point Tracking (MPPT) technique. The MPPT technique determines the voltage of the PV module in order to extract the maximum solar energy.

3.1 Photovoltaic generator

The building block of PV arrays is the solar cell, which is basically a (p-n) semiconductor junction that directly converts light energy into electricity. The equivalent circuit of a PV cell described by the one diode is as shown in Fig. 3. The current source I_{ph}, represents the cell photocurrent; Rd is used to represent the nonlinear impedance of the (p-n) junction; R_{sh} and R_s are the intrinsic shunt and series resistances of the cell, respectively. Usually the value of R_{sh}, is very large and that of R_s, is very small, hence they may be neglected to simplify the analysis [9], [10].

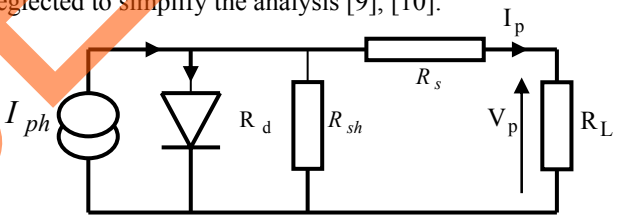

Fig. 3: Equivalent Circuit of a Solar Array.

The current output of a photovoltaic cell *Ip* can be modeled mathematically using Eq.1.

$$I_P = I_{Ph} - I_s\left[\exp\left(\frac{V_p + R_s \cdot I_P}{V_T}\right) - 1\right] - \frac{V_p + R_s \cdot I_P}{R_{sh}} \quad (1)$$

Where, $V_T = \frac{n.K_B.T}{q}$ is the thermodynamic voltage.

PV cells are grouped in larger units called PV modules which are further interconnected in a parallel-series (N_p-N_s) configuration to form PV arrays or PV generators. The PV array current can be calculated using Eq.2.

$$I_P = N_p\left[I_{Ph} - I_s\left[\exp\left(\frac{1}{V_T}\left(\frac{V_p}{N_s}+\frac{R_s \cdot I_P}{N_p}\right)\right)-1\right]\right] - \frac{N_p \cdot V_p}{N_s \cdot R_{sh}} - \frac{R_s \cdot I_P}{R_{sh}} \quad (2)$$

For the bond graph representation, the PV generator is then modeled by a flow source $S_f = I_{ph}$ in parallel with two resistors R_d and R_{sh}, the whole followed by a serial resistance R_s. The PV diode bond graph representation is a non-linear resistor Rd whose current-voltage relation is a non linear (2). We use in a first stage a standard equivalent circuit composed of a PV generator coupled to a resistive (R_L) load.

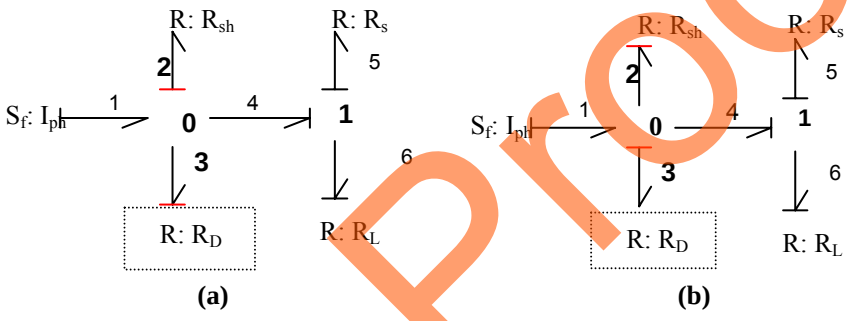

Fig. 4. Bond Graph model of PV generator with conductance causality for Rd (a), resistance causality for Rd (b).

As illustrated on Figs. 4, the Bond Graph formalism illustrates the causality assignment via the "causal stroke" which indicates the direction in which the effort (voltage in electricity) is imposed [9].

Two different causality assignments in bond 2 and 3 can be performed. In fact, Rd and Rsh introduce an uncertainty in the causal structure creating numerical problems (algebraic loop) linked to implicit equations corresponding to conductance causality for Rd (Fig. 4a) or resistance causality for Rd (Fig. 4b). The detection of this double causality affectation before doing numerical resolution phase puts in evidence one of the interesting features of bond graph modeling. To solve this problem of causal loop, it is why a simplification of the PV generator model. The representation by a reduced model consists often in neglecting resistances Rs which avoids the implicit equations and facilitate considerably the exploitation of PV generator for minimizing computing time.

The bond graph model obtained is well adapted for simulation since there is no algebraic loop. The model is characterized by a modulated source flux determined by the solar power associated to in parallel with two resistors Rd and Rsh [3]. Thus, this model remains representative of the physical phenomena of the PV cell (resistive drop and recombination in particular) while being inexpensive in computing times. The inputs of this model are radiation and the temperature. The output variable is regarded as a nonlinear electric current source (Fig. 5).

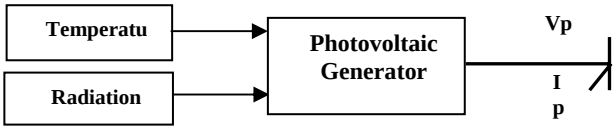

Fig. 5: Global Bond Graph model of PV generator

This model is solved by 20-sim Bond Graph software. Fig. 6 shows a typical current-voltage and power-voltage characteristics of this PV generator model. These characteristics depend on the solar radiation and on the temperature of the solar cells.

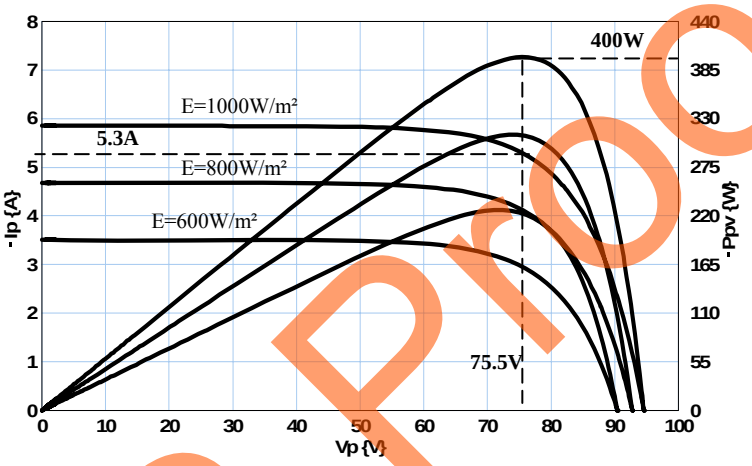

Fig. 6 : Example of current-voltage, power-voltage characteristics of a photovoltaic module in function of the solar radiation.

3.2 Buck converter model

The commutation cell can be represented according to many models, corresponding to objectives, degrees of refinement and thus at distinct simulation cost. This representation is more crucial as the static converters with spontaneous or forced commutation are often responsible for the fastest modes, therefore more "expensive" in simulation of the power electric systems. From an analysis point of view it is convenient to use averaged bond graph model of buck converter [8, 9].

In the Fig 7 can be seen a principle scheme for a buck converter. For buck converter presented below is presumed that is working in continuous-conduction mode.

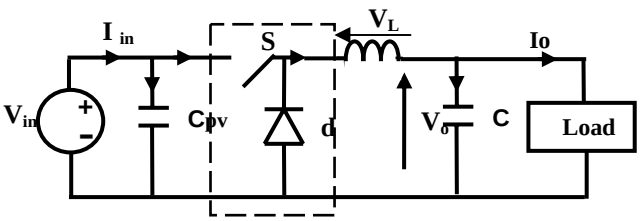

Fig. 7: Buck (DC-DC) converter

A Buck converter operates in continuous mode if the current through the inductor (I_o) never falls to zero during the commutation cycle. In this mode, the operating principle is described by the chronogram on Fig 8.

By varying the duty-cycle $\frac{T_{on}}{T}$ of the switch, V_0 the output voltage can be controlled. The voltage on the diode is fluctuating between 0 and V_{in}, but this is not acceptable in most of the applications. For this reason an inductor is necessary.

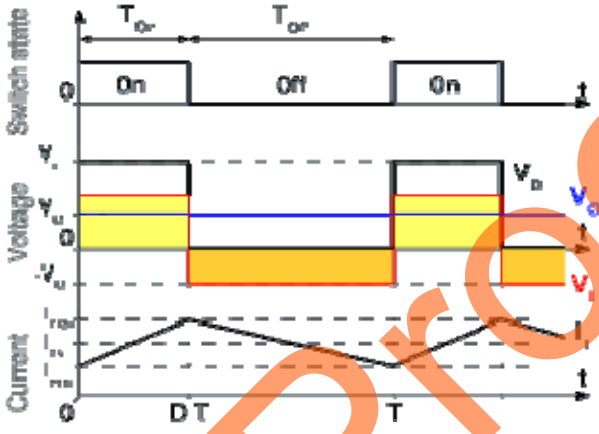

Fig. 8: Evolution of the voltages and currents in an ideal Buck converter operating in continuous mode.

In continuous-conduction mode, since in steady state the time integral of the inductor voltage over one time period must be zero. Consequently, in average value over the switching period (T), we have the following equation:

$$(V_{in} - V_o).T_{on} = V_o.(T-T_{on}) \quad (3)$$

where,

$$\frac{V_o}{V_{in}} = \frac{T_{on}}{T} = D \quad (4)$$

This means that the output voltage varies linearly with the duty-cycle. Assuming a lossless circuit, the input power P_{in} must be equal to the output power P_o.
It yields,

$$V_{in}.I_{in} = V_o.I_o \quad (5)$$

and,

$$\frac{I_o}{I_{in}} = \frac{V_{in}}{V_o} = \frac{1}{D} \quad (6)$$

Therefore, in the continuous-conduction mode, the Buck converter is equivalent to a DC transformer whose the turn ratio can be continuously controlled in a range from 0 to 1. The Bond Graph model of the Buck converter is depicted in Fig 9. The commutation cell model has been taken as a modulated transformer, which has the same behavior as an ideal switch for an averaged model:

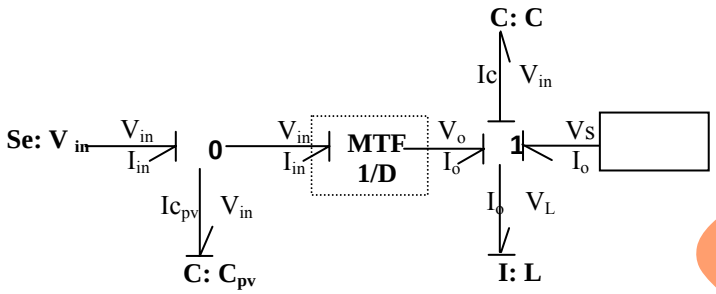

Fig. 9: Averaged Bond Graph model of Buck (DC-DC) converter

3.3 Design equation of the inductance (L) and capacitors (C_{pv}, C)

The inductance value required to operate the converter in the continuous conduction mode is calculated such that the peak inductor current at maximum output power does not exceed the power switch current rating. Thus, the inductance value can be calculated by Eq.7.

$$L = \frac{V_{o\max} \cdot (1 - D_{\max})}{f_s \cdot |\Delta I_{L\max}|} \tag{7}$$

where

$f_s = \frac{1}{T}$ switching frequency;

D_{max} duty cycle at maximum converter output power;

ΔI_{Lmax} peak-to-peak ripples of the inductor current;

V_{omax} maximum of the DC component of the output voltage;

I_{omax} DC component of the output current at maximum output power;

The output capacitor value calculated to give the desired peak-to-peak output voltage ripple is:

$$C = \frac{I_{o\max} \cdot D_{\max}}{f_s \cdot |\Delta V_{L\max}|} \tag{8}$$

where

ΔV_{omax} output voltage peak-to-peak ripple at maximum power;

Taking into account that the ripple of the PV output current must be less than 2% of its mean value, [12], the input capacitor C_{pv} value is calculated to be:

$$C_{pv} = \frac{I_{o\max} \cdot D_{\max} \cdot (1 - D_{\max})}{0.02 \cdot V_{in\max} \cdot f_s} \tag{9}$$

where

V_{inmax} PV array output voltage at maximum power point;

When the Buck converter is used in PV subsystem, the input power, voltage and current change continuously with the atmospheric conditions, thus the converter conduction mode changes since it depends on them. Also, the duty cycle D is changed continuously in order to track the maximum power point of the PV array. The choice of the converter switching frequency and the inductor value is a compromise between converter efficiency (losses), cost, power capability and weight. For example, the higher the switching frequency, the

lower the inductor core size, but the power switch losses are higher. Also, by using a large L value, the peak-to-peak current ripples ΔI_L is smaller; requiring lower current rating power switches, but the converter size is increased substantially because a larger inductor core is required.

3.4 Buck Losses model

The Buck converter model presented as a modulated transformer is an ideal element that does not refract actually the energy conversion. For this, we have investigated to the refinement of the buck model by predicting and integrating the IGBT and diode conduction and switching losses in the Buck model [5] [13].

A. Conduction losses model

The conduction losses are due to the device conduction characteristics. The conduction losses are function currents and depend on device characteristics. To find out the device conduction losses, we need to model the device static I-V characteristics. Their information is usually available from manufacturer's data sheets. Fig. 10a, Fig b shows the piecewise characteristics of IGBT and diode [14, 15].

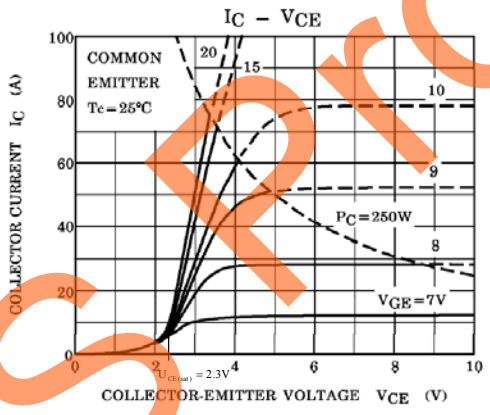

(a)

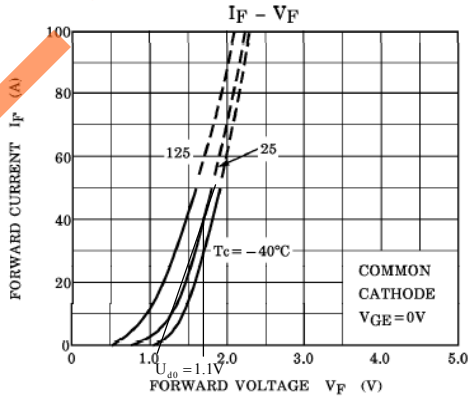

(b)

Fig. 10: Characteristics of IGBT (a) and diode (b)

Conduction losses in the semiconductor devices are then approximated using a piece-wise linear approximation of the device's on-voltage characteristics. The typical IGBT voltage/current graph V_{ce}-I_c is approximated by the following linear equation:

$$V_{CE} = U_{CE(sat)} + R_d \times I_c \tag{10}$$

Where, $U_{CE\ (sat)}$ and R_d are the voltage and the dynamic resistor of IGBT. In this case, we work with the characteristic of IGBT corresponding at V_{GE} =15V.At the same way, the diode forward voltage characteristic can be approximated by means of a linear law with the origin at the threshold voltage U_{d0}:

$$V_F = U_{d0} + R_{d0}.I_F \tag{11}$$

where, R_{d0} is the dynamic resistor of diode which can be determined by setting (I-V) characteristics curves.

The average conduction power loss IGBT and diode for one switching period cycle can be expressed respectively as follows:

$$\left\langle P_{IGBT\_cond} \right\rangle = \left\langle V_{CE} \right\rangle \left\langle I_o \right\rangle D \tag{12}$$

$$\left\langle P_{diode\_cond} \right\rangle = \left\langle V_F \right\rangle \left\langle I_o \right\rangle (1-D) \tag{13}$$

B. Switching losses model

The switching losses are a function of the switching frequency, the current in each device, and the device's dynamic characteristics. Switching losses include IGBT turn-on loss, turn-off loss and reverse recovery loss. Fig. 11 shows approximate waveforms for the hard turn-on transient of an IGBT. The turn-on loss is calculated according to the voltage and current waveform during the turn-on / turn-off transition. Eq.14 gives the average turn-on loss energy is as follows:

$$W_{on} = \int_0^{t_{on}} I_T(t) \cdot U_T(t) \cdot dt \tag{14}$$

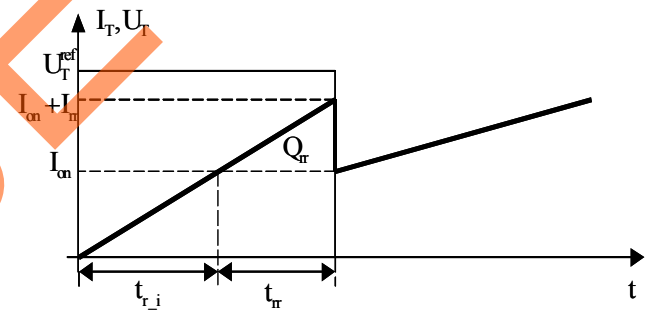

Fig. 11: Hard-switching turn-on transient waveforms

As the voltage of the IGBT gate-emitter U_T increases above the threshold voltage U_T^{ref} at time (t_{r_i}+ t_{rr}), the IGBT current increases at a rate dependant on the rail voltage and the stray inductance. Simultaneously, the IGBT collector voltage drops to a level determined by the circuit stray inductance. As the IGBT current reaches the load current

level I_{on} at time t_{r_i}, the associated free-wheeling diode begins to reverse recovery with Q_{rr} reverse recovery charge. According to Fig. 11, the total IGBT turn-on loss can be approximated by Eq.15.

$$W_{on} = \frac{U_T^{ref}(I_{on} + I_{rr}).(t_{r\_i} + t_{rr})}{2} \tag{15}$$

Where I_{rr} is the peak reverse recovery current of the free-wheeling diode and t_{rr} is the reverse recovery time of the diode. In Eq.12, parameters t_{rr} and I_{rr} depend on the properties of the free-wheeling diode, which means the IGBT turn-on loss can be affected significantly by properties of the free-wheeling diode.

Turn-off approximate waveforms of the IGBT are shown in Fig 12. Eq.16 gives the average energy lost during transistor turn- off transition:

$$W_{off} = \int_0^{t_{off}} I_T(t) \cdot U_T(t) \cdot dt \tag{16}$$

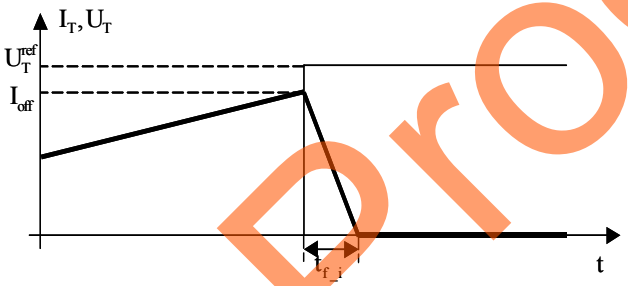

Fig. 12: Typical hard switching turn-off transient waveforms.

During t_{f_i}, collector-gate current decreases rapidly, which results in a rapid collector voltage increase. After it reaches the rail voltage U_T^{ref}, the free-wheeling diode (df) is activated and the IGBT current drops rapidly to a level determined by the total stored charge inside the device. The decay rate of the tail current that follows depends on the carrier lifetime in the IGBT base and the reverse injection efficiency of the anode-base junction. According to Fig. 12, the total turn-off loss can be approximated by Eq.17.

$$W_{off} = \frac{U_T^{ref} \cdot I_{off} \cdot t_{f\_i}}{2} \tag{17}$$

The turn-off time tf_i parameter shown in Eq.14 is highly dependant on the properties of the IGBT giving by manufacturer's data sheet.

The average total IGBT switching losses (on + off) could be estimated by multiplying the energy loss of each switching operation with the switching frequency:

$$\left\langle P_{IGBT\_switch} \right\rangle = (W_{on} + W_{off}) f_{sw} \tag{18}$$

where f_{sw}: switching frequency

For the averaged model, we can suppose that: $I_{on} = I_{off} = I_o$, $U_T^{ref} = V_{in}$ (Where I_o and V_{in} are respectively the output current and the input voltage of buck converter).

The total power losses buck converter result respectively during switching period:

$$\left\langle P_{total\_loss} \right\rangle = \left\langle P_{IGBT} \right\rangle + \left\langle P_{diode} \right\rangle \quad (19)$$

Fig. 13 (a), 13(b) present an average bond graph model of buck converter, taking into account the total switching and conduction losses calculated before. The total power losses is then modelled by a modulated effort source MSe = f(V_{in},I_o,D), Fig. 13 (a) or with a modulated resistor MR= f(V_{in}, I_o,D) Fig. 13 (b).

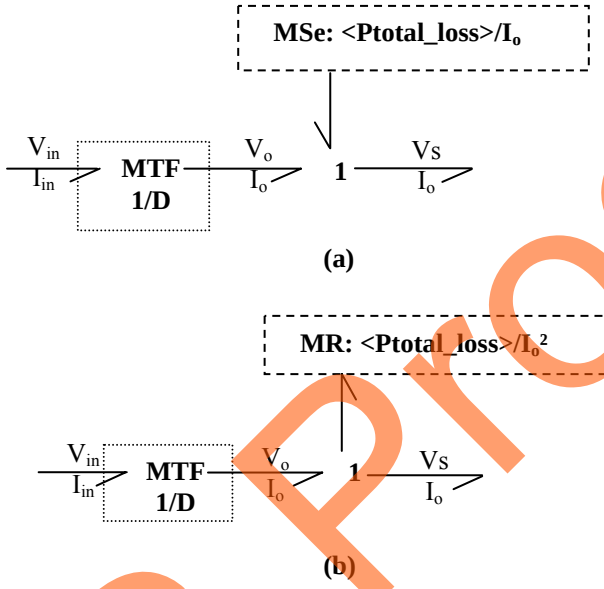

Fig. 13: Averaged Bond Graph model of Buck (DC-DC) converter including losses: (a) modulated effort source MSe, (b) modulated resistor MR

3.5 Control strategy of PV subsystem

The aim of the control strategy is to adjust the voltage V_p to have the maximum power extraction. The duty cycle D_{pv} is the control parameter. From the Fig. 14, it can be deduced that two controllers must be considered to control respectively the array voltage V_p and the PV output current I_o by taking into account the MPPT algorithm, the control strategy shown in Fig. 14 is naturally deduced from the proposed PV subsystem model:

$$\frac{dV_p}{dt} = \frac{1}{C_{pv}}(I_p - D_{pv} \cdot I_o) \quad (21)$$

$$\frac{dI_o}{dt} = \frac{1}{L}(D_{pv} \cdot V_P - V_{bat}) \quad (22)$$

Fig. 14 shows the MPPT technique using open circuit voltage of PV-module in small-scaled PV-power system. This method uses the fact that the operating voltage (V_{op}) at MPP of PV-module is near linearly proportional to open circuit voltage (V_{oc}) of PV-module [9].

$$V_{op} = k_v \cdot V_{oc} \quad (23)$$

where, the proportional constant (k_v) is about 0.78(± 2%).

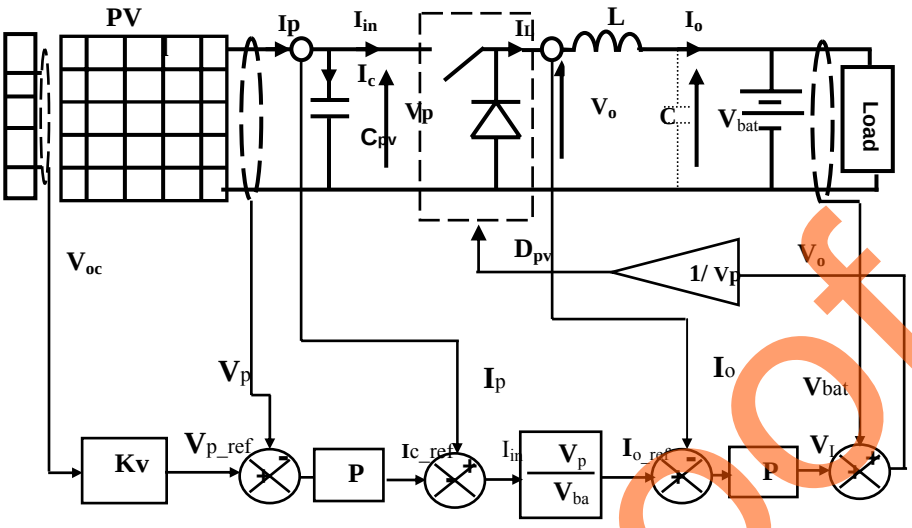

Fig. 14: PV subsystem control diagram.

4. WIND ENERGY CONVERSION SUBSYSTEM

The bloc diagram of the proposed MPPT control for the wind subsystem adopted in this paper is shown in Fig. 2. It consists of a small wind turbine coupled to a permanent magnet synchronous generator (PMSG), the output voltage and frequency from the generator will vary for different wind velocities. The variable output AC power from the generator is first converted into DC using an uncontrolled diode bridge rectifier. A buck converter is used to match the variable DC voltage with the DC bus and to track maximum power available from the wind energy system for a given wind velocity and deliver this power to a 48 V DC constant voltage load. The voltage across the rectifier terminal is controlled by varying the duty cycle of the (DC/DC) converter before it is fed to the DC bus.

The system is designed to control the output current I_w. By measuring the DC rectifier voltage V_{dc}, the reference current is calculated with the MPPT loop. The optimal reference value of the current I_{ref_w} is imposed to the current controller of the (DC/DC) chopper [4] [16]. The error resulting from the comparison between desired and actual values of the output current I_w is processed by the microcontroller through a PI regulator, issuing a value V_L of the inductance voltage (L). The sum of the inductance voltage V_L and the battery voltage V_{bat} is divided by DC voltage V_{bus} to issue the duty-cycle D_w required for the IGBT switching operation, as shown in Fig. 15.

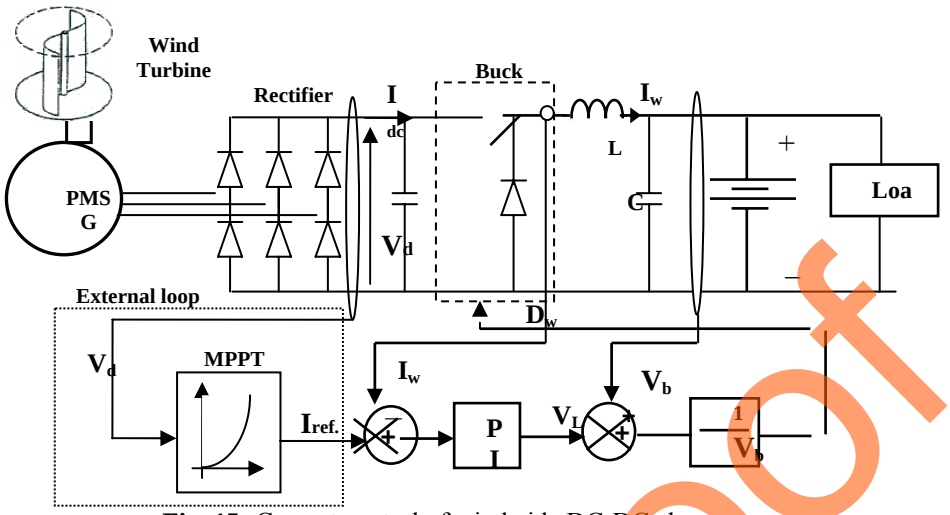

Fig. 15: Current control of wind-side DC-DC chopper

4.1 Wind turbine

The output mechanical power of the wind turbine is given by the usual cube law equation

$$P_w = 0.5 \cdot C_p \cdot \rho \cdot \pi R^2 \cdot V_w^3 \quad (24)$$

Where V_w is the average wind velocity (m/s), ρ is the air density (kg/m^3), R is the radius of the turbine blades (m) and C_p is the power coefficient, which is a function of the tip speed ratio λ given by Eq.25.

$$\lambda = \frac{\omega_m R}{V_w} \quad (25)$$

Where ω_m is the rotor mechanical speed (rad/s).
The output torque T_w of the wind turbine is calculated from the following equation:

$$T_w = \frac{P_w}{\omega_m} = \frac{0.5 \cdot C_p \cdot \rho \cdot \pi R^3 \cdot V_w^2}{\lambda} \quad (26)$$

4.2 Model of the permanent magnet synchronous generator (PMSG), rectifier and buck

A 600W, 34 pole, 300 rpm rated speed, permanent magnet synchronous generator (PMSG) is employed in the wind subsystem. The generator output voltage varies according to the wind speed variation. Hence, the 3-phase output of the PMSG is rectified with a full wave diode bridge rectifier, filtered to remove significant ripple voltage components, and fed to (DC/DC) buck converter. For an ideal (unloaded and loss-less) PMSG, the line to line voltage is given as [17]:

$$V_L = K_v \omega_e \sin(\omega_e t) \quad (27)$$

Where K_v is the voltage constant and ω_e is the electrical frequency related to the mechanical speed ω_m by:

$$\omega_e = \omega_m \cdot \left(\frac{n_p}{2}\right) \quad (28)$$

where n_p is the number of poles of the PMSG.

Neglecting commutation delays, the DC rectifier voltage V_{dc} is given as:

$$V_{dc} = \frac{3\sqrt{2}}{\pi} \cdot V_{Lrms} - \frac{3\omega_e L_s}{\pi} I_{dc} \quad (29)$$

Where V_{Lrms} is the rms value of the PMSG output voltage, I_{dc} is the average rectifier PMSG output current and L_s is the stator inductance. Neglecting the generator and rectifier losses, the PMSG output rectified electrical power P_{dc}, is equal to the mechanical power input to it

$$P_{dc} = V_{dc} I_{dc} \quad (30)$$

The Buck model is developed in PV subsystem section 3.2 and losses models in section 3.4

4.3 Design equation of the DC bus capacitor C_{bus}

The wind generator AC output voltage is first converted to DC form using a three-phase full-wave bridge rectifier. The rectifier output capacitor value C_{bus} is calculated as follows [12]:

$$C_{bus} = \frac{1}{12 \cdot f \cdot R_L} \left(1 + \frac{1}{\sqrt{2} RF} \right) \quad (31)$$

Where R_L is the wind generator load resistance, f is the wind generator output voltage frequency, and RF is the rectifier output voltage ripple factor.

For the design equation of the inductor L and the capacitor C are similar that in PV buck section 3.3 (respectively equations (7), (8)).

4. 4 MPPT control of the wind subsystem

At any given wind speed, torque vs. rotor speed curves can be easily converted into curves of current vs. speed because of the linear relationship between the electromagnetic torque and the machine phase current. Then, in the current-speed plane it is found that, as the wind speed changes, the point of maximum power operation moves along a curve which can be represented by an expression such as [3]:

$$I_{w.ref} = K_w \cdot \omega_m^3 \quad (32)$$

Where K_w is constant which depend on the wind turbine topology. Therefore, for the output current I_w of the wind-generator-fed converter- buck stage a reference value $I_{w.ref}$ can be calculated from Eq.1 whenever the actual value of the rotor speed ω_m is know. This can be derived from measuring the generator rectified line-to-line output voltage V_{dc}, as it can be written with neglecting rectifier loss as:

$$\omega_m = \frac{\pi \cdot \sqrt{6}}{18 . \phi_v . n_p} V_{dc} \quad (33)$$

Then, the reference value $I_{w.ref}$ is calculated as:

$$I_{w.ref} = K_w \cdot \left(\frac{\pi \cdot \sqrt{6}}{18 . \phi_v . n_p} V_{dc} \right)^3 = K'_w \cdot (V_{dc})^3 \quad (34)$$

The analytic expression of the maximum power that can be produced by the wind subsystem under the optimal power coefficient is expressed according to wind speed as fallowing [3]:

$$P_{w.max} = V_{bat} \cdot K_w \cdot \left(\frac{\lambda \cdot V_w}{R} \right)^3 = K''_w (V_w)^3 \quad (35)$$

5. BATTERY BANK MODEL

The DC load of the hybrid system was arranged by using lead-acid battery and power resistors. The simplified battery bank equivalent circuit is shown in Fig. 16**.** The battery bank may be represented as a voltage source E_b connected in series with a resistance R_b and capacitance C_b [18].

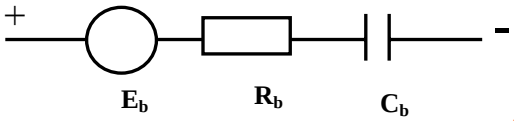

Fig. 16: Battery Equivalent Circuit

Fig. 17 presents a bond graph model of a lead-acid battery corresponding to the electrical equivalent circuit.

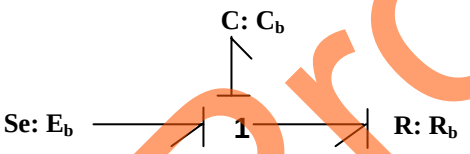

Fig. 17: Equivalent Bond Graph model of lead-acid batteries

6. HYBRID SYSTEM PERFORMANCE

The developed model of the hybrid system shown in Fig.1, associated to the proposed MPPT control of photovoltaic and wind subsystems, summarized in Fig. 14 and Fig. 15, has been numerically simulated by using the Bond Graph environment of 20-sim software.

The performance of the proposed photovoltaic subsystem MPPT control has been evaluated both in steady state and transient operating conditions determined by start up and solar irradiance variations. We simulated the PV subsystem during a cloudy passage: the radiation decreases by 50% and then increases by 50% Fig. 18.

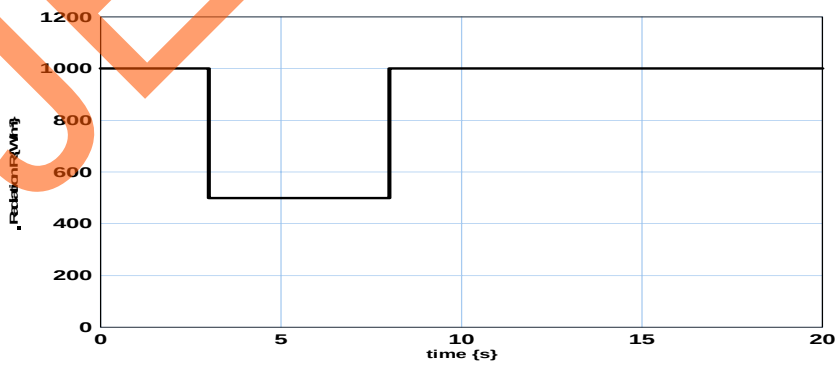

Fig. 18: Solar irradiance variations

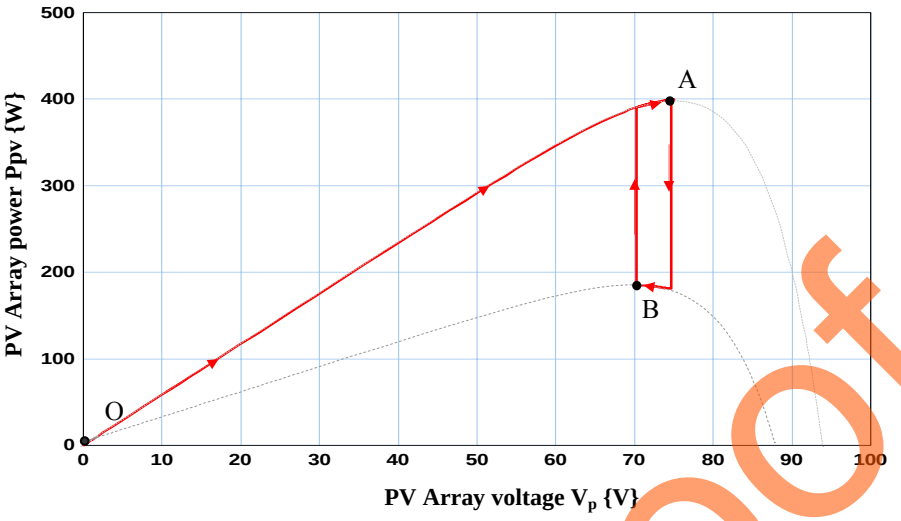

Fig.19: Effect of a -50% and +50% solar irradiance transient on the P_{pv}-V_p diagram

Fig. 19 represents the PV subsystem characteristics on the Ppv-Vp diagram. Fig.19 show the performance of the PV generation subsystem in tracking the maximum power point of the PV panels during a transient of solar irradiance. From the starting operating point O, the system reaches the MPP in A. Then, as a consequence of a 50% reduction in the solar irradiance, the operating point moves to the new MPP in B. When, the solar irradiance increase by 50%, the operating point moves to the first MPP in A. Once the new MPP is reached, only very small oscillations persist around the MPP.

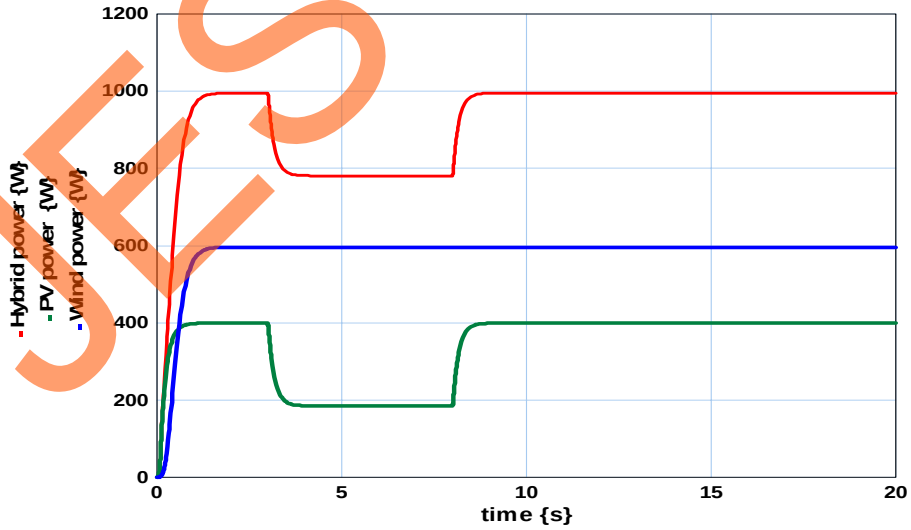

Fig.20 : PV, wind and Hybrid powers

Fig. 20 shows the time behavior of the PV, wind and Hybrid powers during the seeking of the new MPP. It can be observed that the PV power reaches the maximum power point

during the solar irradiance variations. For a wind speed Ws=16m/s, the wind subsystem produces the maximum power (600W). The hybrid power delivered to DC load is well the sum of both sources.

We are interested in this simulation for the analysis of the wind conversion subsystem performance. A comparison of the maximum output wind power obtained in static mode calculated from Eq.35 and the "maximized" output wind power obtained in dynamic mode by using MPPT loop (Fig.15), is given in Fig. 21 corresponds to wind speed varying around 12m/s.

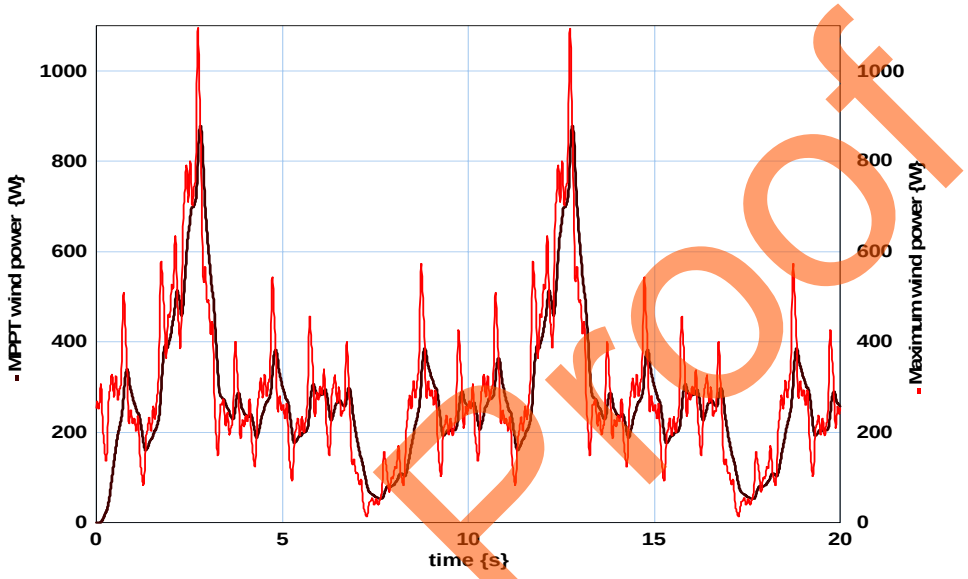

Fig. 21: Maximum wind power (static mode) and MPPT output wind power

The obtained results show the energy effectiveness of the wind subsystem with integration of the losses system. Indeed, the follow-up of the power is very correct what the graphics of the Fig.21 confirm. The difference between the maximum power (mode static) and maximized by MPPT loop does not seem however to be very significant.

Thereafter, we examine the performance of hybrid system with the integration of global losses model in power converters. Simulation results showing the PV subsystem buck efficiency is defined as:

$$\eta = \frac{P_o}{P_{in}} = \frac{P_o}{P_o + P_{losses}} \tag{36}$$

Where P_{in} and P_o are the (DC/DC) converter input and output power, respectively, while P_{losses} is the total power losses.

The theoretical values were calculated using data given by the manufacturers of the circuit elements. The theoretical efficiency for various output power levels is shown in Fig. 22. It is seen that the efficiency is quite high (98%) and relatively constant for a wide output power range.

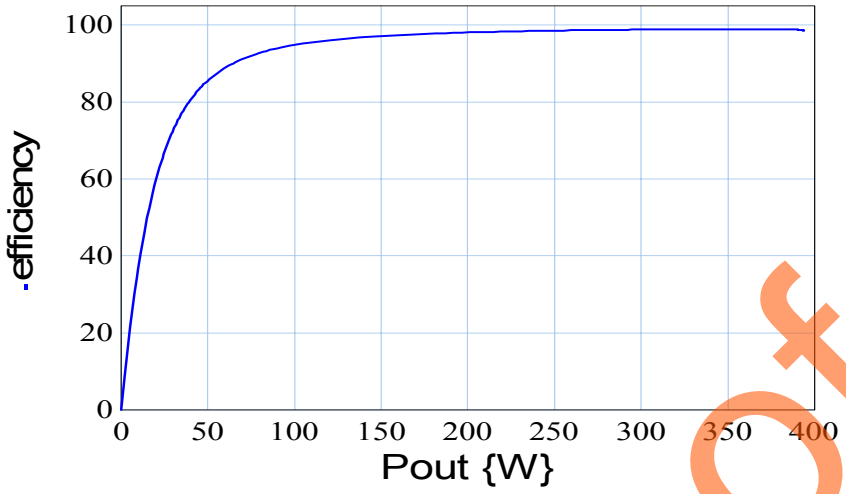

Fig. 22: PV subsystem efficiency under PV MPPT conditions

Fig. 23, Fig. 24 show the active power exchanged with the 48V battery when the wind turbine and the solar generators are connected together to the DC bus. Fig. 23 is characterized by an optimum climatic conditions (Wind speed Ws=16m/s, radiation R = 1kw/m², Temperature T=25°C). Fig. 24 corresponds to wind speed varying around 12m/s and for the same solar climatic condition. These simulations show that the dynamic of the global system is well reproduced by the proposed average continuous model and the importance to include the converters power losses analyses. The objective is to show the real transfer of power flux energy in each part of the hybrid system.
This result must be introduced into account for a very large scale time energy evaluation.

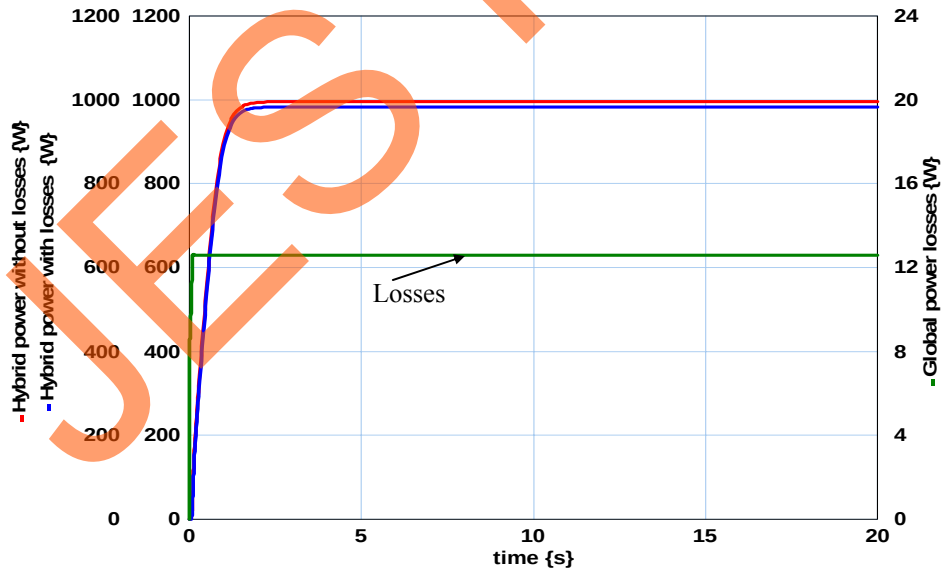

Fig. 23: Hybrid power with losses and without losses for optimum climatic conditions

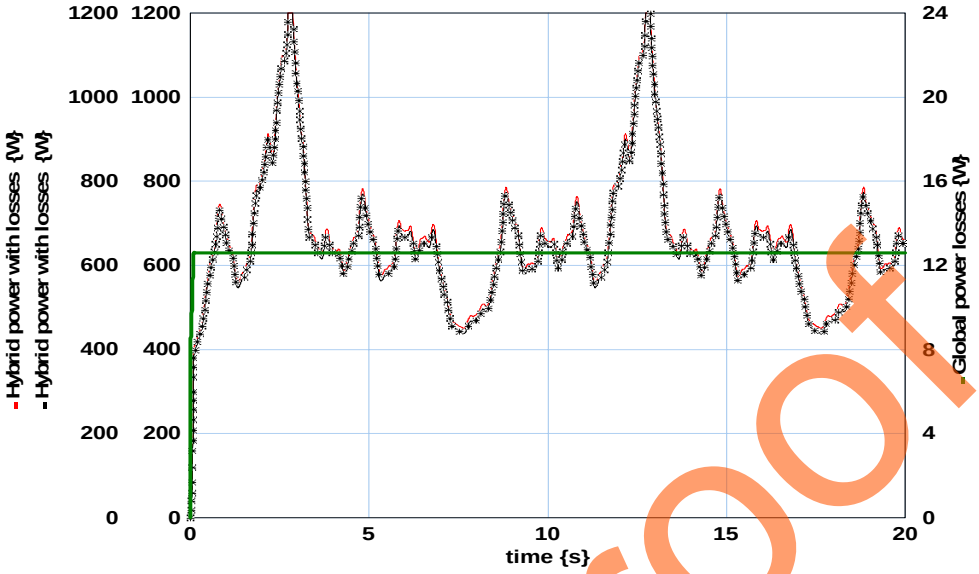

Fig. 24: Hybrid power with losses and without losses for variable wind velocity

7. CONCLUSION

Feasibility study on power control of hybrid PV-wind generation system was conducted at designing stage of the multiple renewable sources hybrid control system. Power electronic interface and its control scheme were proposed for the maximum power generation of the hybrid PV-wind system with battery interface. The dynamic analysis models of the hybrid system components and power control schemes were addressed in this paper. The model of the solar generating subsystem and wind subsystem has been developed with integration of power losses model involved in the power converters. It has been shown that this model is interesting for analyzing the dynamic behavior and for an optimum designing of the hybrid system. The key prerequisite for improving system performance understands operating characteristics including losses. Therefore, a prediction losses method has been developed that is especially designed to analyze the performance of hybrid power system and witch's interesting for long time dynamic simulations and experimental validation work. Included in the analysis are power loss models that are required for prediction of system efficiency and for develop realistic balance energy between powers produced by the sources, demanded by the load and stored in battery.

The MPPT controls system has developed for both sources. The objective is to track the maximum power for the DC load. The PV subsystem management is based on cascaded voltage-current control. For, the wind subsystem a current control is used. Modeling and simulation study on the entire control scheme is carried out using a power system transient analysis Bond Graphs tool. The simulation results showed the excellent performance of the hybrid PV-wind control in response to severe changes in wind speed and solar intensity conditions.

References

[1] T. Senjyu, T. Nakaji, K. Uezato and T. Funabashi, A hybrid System Using Alternative Energy Facilities in Isolated Island, IEEE Trans. Energy Conversion, vol. 20, no. 2, pp. 406-414 June 2005.

[2] F. Giraud, and Z. M. Salameh, Steady-state performance of a grid connected rooftop hybrid wind-photovoltaic power system with battery storage, IEEE Transactions on Energy Conversion, Vol. 16, No. 1, March 2001, pp.1-7.

[3] M. Dali, J. Belhadj and X. Roboam, Design and control of hybrid Photovoltaic -Wind systems, RIGE, vol. 9/6, pp.719-752, December 2006.

[4] M. Dali, J. Belhadj, X. Roboam, Control and energy management of a wind-photovoltaic hybrid system, 12th European Conference on Power Electronics and Applications - EPE 2007, 2-5 September 2007, Aalborg, Denmark.

[5] M. Dali, J. Belhadj and X. Roboam, Design and Energy based model of stand-alone hybrid Photovoltaic-Wind generating system with integration of converter losses, International Conference on Electrical Engineering Design and Technologies (ICEEDT), November 4-6, 2007, Hammamet, Tunisia.

[6] A. Ben Rhouma J.Belhadj X.Roboam, Design and control of a pumping system fed by hybrid Photovoltaic-Wind source without battery storage, International Conference on Electrical Engineering Design and Technologies (ICEEDT), November 4-6, 2007, Hammamet, Tunisia.

[7] M. Turki J. Belhadj X. Roboam, Design and Energy management of a small-scale reverse osmosis desalination unit powered by PV-Wind hybrid system without battery storage, International Conference on Electrical Engineering Design and Technologies (ICEEDT), November 4-6, 2007, Hammamet, Tunisia.

[8] X. Roboam, and S. Astier, Les Bond Graphs causaux pour les systèmes à énergie renouvelable, Techniques de l'ingénieur, D3910, 2006.

[9] M. A. S. Maoum, S. M. M. Badejani and E. F. Fuchs, Microprocessor -Controlled New Class of Optimal Battery Chargers for Photovoltaic Applications, IEEE Trans. Energy Conversion, vol. 19, no.3, pp. 599-606, Sep., 2004.

[10] Dong-Yun Lee., Hyeong-Ju Noh., Dong-Seok Hyun and Ick Choy, An Improved MPPT converter using current compensation Method for small scaled PV-Applications IEEE Transactions on Energy Conversion, 2003,pp 540-545.

[11] O. Al-Naseem, R.W. Erickson, and P. Carlin, Prediction of switching loss variations by averaged switch modelling, Applied Power Electronics Conference and Exposition, APEC 2000. Fifteenth Annual IEEE, vol 1, pp. 242 – 248, Feb. 2000.

[12] E. Koutroulis and K. Kalaitzakis , Design of a Maximum Power Tracking System for Wind- Energy-Conversion Applications, IEEE transactions on industrial electronics, vol. 53, no. 2, pp 486-494, april 2006.

[13] N.K. Lujara,; J.D. van Wyk, and P.N. Materu, Power electronic loss models of DC-DC converters in photovoltaic applications, Industrial Electronics, 1998. Proceedings. ISIE '98. IEEE International Symposium on Volume 1, 7-10 July 1998 Page(s):35 - 39 vol.1

[14] A. Mirecki, Comparative study of energy conversion chains dedicated to a small scaled wind power, Ph.D. Thesis, Dept, Elect, Univ. ENSEEIHT- INPT, Toulouse, April 2005.

[15] IGBT Characteristics, International Rectifier note, AN-983.

[16] A. Mirecki, X. Roboam and F. Richardeau, Architecture cost and energy efficiency of small Wind Turbines : which system tradeoff?, IEEE Transactions on Industrial Electronics, Vol 54, N°1, pp 660 – 670, February 2007.

[17] MJ. Ryan and RD. Lorenz, A novel control-oriented model of a PM generator with diode bridge output, Proceedings of EPE conference, Trondheim, Norway, 1997, p. 1.324–1.329.
[18] Z.M. Salameh and B.S. Borowy, Dynamic Response of a Stand- Alone Wind Energy Conversion System with Battery Energy Storage to a Wind Gust, IEEE Transactions on Energy Conversion, Vol. 12, Mars 1997.